



Synthesis process and thermoelectric properties of the layered crystal structure SnS₂

Yi Chang^{1,3} · Min Ruan^{1,2} · Fu Li¹ · Zhuanghao Zheng¹ · Yuexing Chen¹ · Zhenhua Ge³ · Ping Fan¹

Received: 24 November 2019 / Accepted: 12 February 2020 / Published online: 22 February 2020
© Springer Science+Business Media, LLC, part of Springer Nature 2020

Abstract

This work reports on the thermoelectric properties of bulk SnS₂, which shows a similar composition and layered crystal structure to the extensively studied SnS and SnSe. The synthesis process for mechanical alloying (MA) SnS₂ was also investigated. The SnS₂ compound was formed in the reaction between SnS and S, after the formation of SnS using Sn and S as raw materials. However, single-phase SnS₂ appears to be difficult to obtain by MA because Sn₂S₃ is produced when milling times are extended. Nevertheless, a pure-phase SnS₂ bulk is achieved by further spark plasma sintering. The pristine SnS₂ bulk shows an n-type conductive characteristic and a moderate absolute Seebeck coefficient between 100 and 700 $\mu\text{V/K}$. However, with a low figure of merit value ZT , the thermoelectric property is poor because of the low electrical conductivity of below 0.2 S/cm and the relatively high thermal conductivity of above 1.5 W/mK. Further, the electrical conductivity is enhanced and the thermal conductivity decreases significantly after Ag doping. An enhanced ZT value of 0.01 is achieved which is two times higher than pristine one.

1 Introduction

Thermoelectric (TE) solid-state energy conversion technology [1–3] has attracted great attention in reducing the energy consumption and enhancing the energy utilization efficiency because of their capability to convert waste heat directly into electricity according to the Seebeck effect—a phenomenon by which a voltage is produced when a material is exposed to a temperature gradient [4, 5]. The TE efficiency of a material used in TE devices is determined by the dimensionless figure of merit, $ZT = S^2\sigma T/\kappa$, where S denotes the Seebeck coefficient, σ the electrical conductivity, κ the thermal conductivity, and T the absolute temperature, respectively. Thus, a large Seebeck coefficient, a high electrical conductivity, and a low thermal conductivity are needed to realize high

ZT values. However, as these three transport coefficients are interdependent, searching for practical materials with good TE performance is challenging [6, 7].

Natural superlattice materials typically consist of two or more periodically stacked sublattices, which often exhibit special physical properties. There remains the possibility that the thermal and electrical properties of these materials may be adjusted independently. Therefore, the idea of a natural superlattice as a means to develop new TE materials has received much interest. Actually, some of the layered materials, such as CaAl₂Si₂-type Zintl compounds [8], SnS [9] WoS₂ [10], and layered Co oxides [11–13], with excellent TE properties, have been developed in recent years. As a typical example, the layered and anisotropic crystal structure of SnSe single crystal brings about an extremely low thermal conductivity, which results in a much higher ZT value of over 2.0 along the b- and c-axis directions [14] and establishes it as a very promising material. Moreover, layered metal dichalcogenides MX₂ (M = W, Ti; X = S, Se), the constituent elements of which are abundant and non-toxic, are also supposed to be good TE materials because of its acceptable Seebeck coefficient and comparatively low cross-section thermal conductivity [15, 16]. Among them, Guilmeau and collaborators reported that TiS₂ shows a high-power factor of 1.7 mW/mK² at 325 K [17]. Here, the power factor (PF) is $\text{PF} = \sigma S^2$, which is always primarily evaluated from the TE

✉ Fu Li
lifli@szu.edu.cn

¹ Shenzhen Key Laboratory of Advanced Thin Films and Applications, College of Physics and Optoelectronic Engineering, Shenzhen University, Shenzhen 518060, China

² College of Materials Science and Engineering, Shenzhen University, Shenzhen 518060, China

³ Faculty of Materials Science and Engineering, Kunming University of Science and Technology, Kunming, Yunnan 650093, China

potential of the material. Recently, Nunna and collaborators further optimized the TE properties of TiS_2 and reported a maximum ZT of 0.54 at 700 K for $\text{Cu}_{0.05}\text{TiS}_{1.5}\text{-Se}_{0.5}$. [18] Moreover, WS_2 was also found to be a good TE material at high temperatures. N-type WS_2 can achieve a maximum ZT value of 0.90 at 1500 K, which is comparable to the best TE materials presently used in devices [19]. As a member of the metal dichalcogenides, tin bisulfide (SnS_2) also crystallizes in hexagonal close-packed CdI_2 -type structure [20]. It has attracted much attention because it is the thinnest two-dimensional crystal structure in the field of energy storage. However, although many promising TE materials have been found in metal dichalcogenides, the experimental reports on the TE properties of SnS_2 are scarce. In fact, according to theoretical calculation, the PF of SnS_2 reaches as high as 11.89×10^{-4} and 15.50×10^{-4} W/mK^2 along the a-axis direction at 800 K, suggesting that SnS_2 might be a very promising TE candidate. Furthermore, bulk SnS_2 shows a similar composition and layered crystal structure as the extensively studied SnS and SnSe , which also indicates that SnS_2 may be a good TE material.

In this work, the TE properties of pure SnS_2 , which was prepared by combining mechanical alloying (MA) with spark plasma sintering (SPS), have been investigated. The synthesis process was also studied considering the results of X-ray diffraction (XRD) patterns and Raman spectrum. With an aim to further improve its TE property, Ag-doped SnS_2 has been prepared. Benefiting from the enhanced electrical conductivity compared with that for a pristine sample, an optimal TE property has been achieved.

1.1 Experimental section

In a typical experiment, commercial powders of Sn (99.99%), S (99.95%), and Ag (99.9%) were used as raw materials to synthesize the pristine SnS_2 and Ag-doped SnS_2 samples. They were weighed according to the nominal composition of SnS_2 - $X\%$ Ag ($x=0,3$) and then milled at 425 rpm for 5–11 h in an atmosphere of high-purity argon (99.99%), using a planetary ball milling machine (QM-2SP2, Nanjing University, China). Stainless steel vessels and balls were used, and the weight ratio of the ball to powders was kept at 30:1. After that, the precursor powders were charged into column graphite dies with diameters of 15 mm and sintered in vacuum environment by a spark plasma sintering system (SPS, LABOX-325, Japan) under a uniaxial pressure of 50 MPa at 723 K for 5 min to obtain the final samples.

The phase structures and compositions of SnS_2 - $X\%$ Ag ($x=0,3$) powders and bulk samples were analyzed in X-ray diffraction (XRD, Rigaku, Japan) with a $\text{CuK}\alpha$ radiation and Raman spectrum (Raman inVia, China). The morphology, elementary composition ratio, and element mappings of the SnS_2 sample were observed using

a scanning electron microscope and an energy-dispersive spectrometer (SEM, EDS, Supra 55 Sapphire, Germany). The Seebeck coefficient and electrical resistivity were measured from 323 to 723 K in a helium atmosphere using a Seebeck coefficient/electrical resistance measuring system (Seebeck, Seebeck 458, Germany). The density was measured using Archimedes' method. The thermal conductivity is calculated from the relation $\kappa = DC_p\rho$, where D is the thermal diffusivity measured using laser flash method (LFA467, Netzsch, Germany), C_p —the specific heat capacity—is calculated using the empirical formula: $C_p = A_1 + A_2 \times 10^{-3}T + A_3 \times 10^5T^{-2} + A_4 \times 10^{-6}T^2 + A_5 \times 10^8T^{-3}$ [21], and ρ is the density.

2 Results and discussion

Figure 1a shows the XRD patterns of precursor powders with different milling times (5–11 h). The standard diffraction patterns of SnS_2 (PDF#23–0677), Sn_2S_3 (PDF#72–0031), SnS (PDF#75–0925), Sn (PDF#04–0673), and S (PDF#99–0066) were plotted for comparison (Fig. 1a). They show that with increasing ball milling time, Sn and S elements reacted and formed the SnS phase initially, and then the SnS_2 phase was synthesized via the reaction between SnS and S. When the ball milling time was prolonged to 10 h, the precursor powder was a mixture mainly composed of SnS_2 , SnS, and Sn. However, when the ball milling time exceeded 10 h and 30 min, a new Sn_2S_3 phase appeared in the XRD pattern of the precursor powder. This indicates that with the extension of ball milling time, the formed SnS_2 might react with the redundant SnS to form Sn_2S_3 . As the ball milling time was further extended to 11 h, the full width at half-maximum of Sn_2S_3 peaked and gradually became narrower, indicating that its crystallinity was gradually enhanced. Thus, this result suggests that the pure phase of SnS_2 is difficult to obtain directly by MA using Sn and S as raw materials because of the production of intermediate compounds SnS and Sn_2S_3 . In addition, the morphologies of the precursor powders with different milling times were observed (Fig. 2). The result indicates that the precursor obtained from a 5 h milling time is mainly composed of coarse grains of 1–5 μm diameter (Fig. 2a). With increasing milling time, grain size decreases with the precursor mostly having grain diameters between 200 nm and 1 μm with ball milling times of 8 h, 10 h, and 11 h (Fig. 2b–d). The grain size is also uniform compared with the powder with a 5 h milling times. Combined with the XRD results, the indication is that the constant accumulation of energy by the MA triggers the reaction to produce the compound. Meanwhile, the crushing and extrusion of the MA also reduces the grain sizes of precursor powders after milling over 5 h. Spark plasma sintering is a flash sintering approach combining high electrical current

Fig. 1 **a** XRD patterns of precursor powders with different milling times (5–11 h). **b** XRD pattern of pure SnS₂ bulk

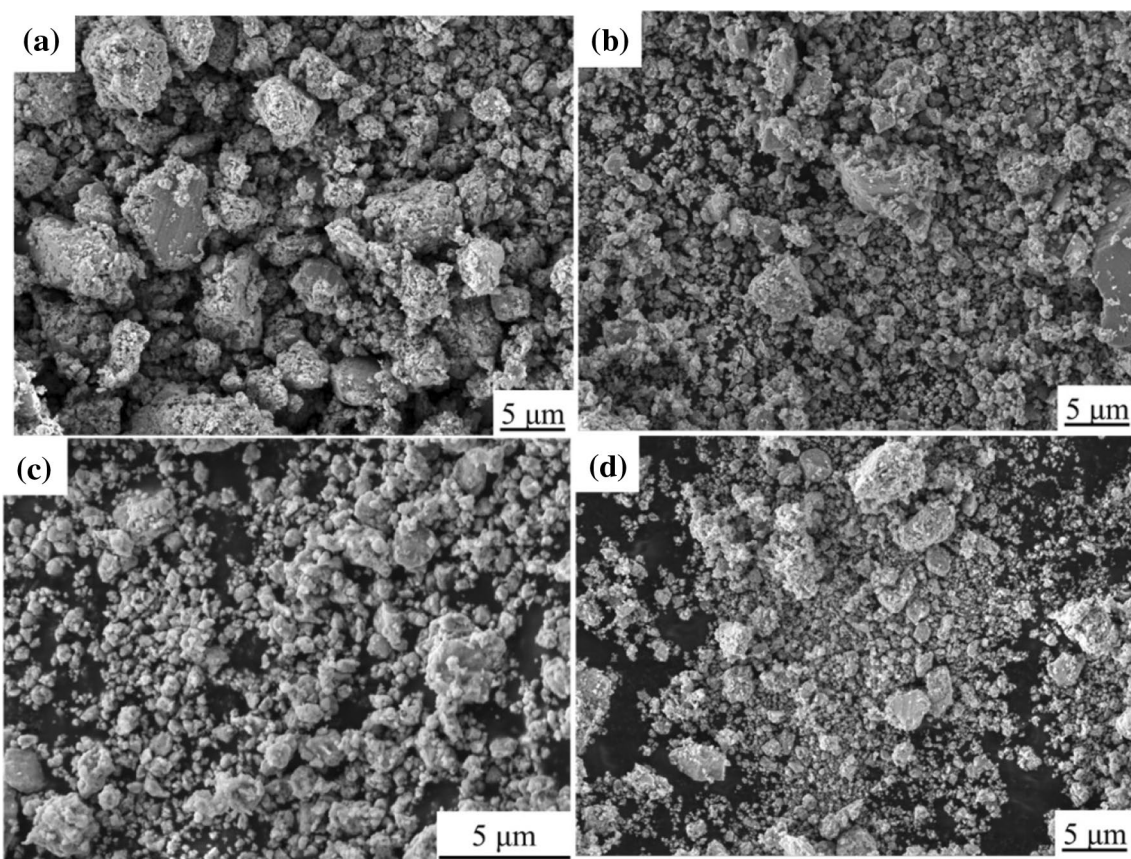
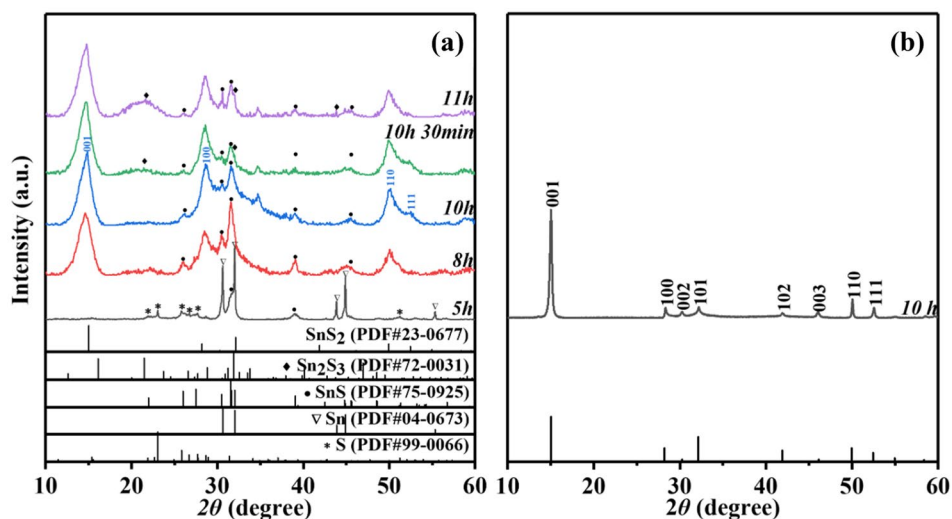


Fig. 2 SEM images for the precursor powders with different milling times. **a** 5 h, **b** 8 h, **c** 10 h, **d** 11 h

and high pressures at the beginning of sintering process; the generated pulsed current can clean the precursor's surfaces form absorb species and create surface defects at the same time, therefore, activating the surface of precursor powders [22]. The activation energy is then significantly reduced,

which assists densification as diffusion, in the form of grain boundary diffusion, lattice diffusion, and volume diffusion, can be accelerated. The sample may also be recrystallized during sintering because of diffusion. Therefore, the precursor powder obtained from a 10 h milling time without the

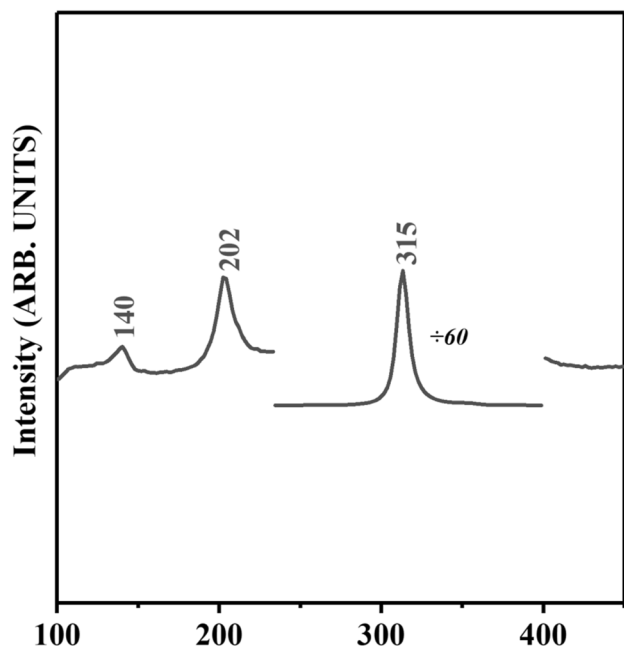


Fig. 3 Unpolarized Raman spectra of pure SnS₂ bulk at 295 K

impure Sn₂S₃ phase was selected for spark plasma sintering to possibly synthesize pure SnS₂ bulk through re-reaction during sintering at high temperature. The XRD pattern for the sintered bulk is exhibited in Fig. 1b. All the peaks can be indexed to the standard diffraction pattern of SnS₂ (PDF# 23–0677); no secondary phase was found, indicating a pure-phase SnS₂ was obtained after sintering. However, it is also found that the relative intensity of the peak (001) is slightly stronger than that of the standard diffraction peak suggesting the existence of anisotropy. Generally, the Lotgering method is used to calculate the *ab* degree of orientation for the (00 *l*) crystal planes in bulk specimen using the following equations, which are referred to as $F_{(00l)}$,

$$F = \frac{P - P_0}{1 - P_0} \quad (1)$$

$$P_0 = \frac{I_0(00l)}{\sum I_0(hkl)} \quad (2)$$

$$P = \frac{I(00l)}{\sum I(hkl)}, \quad (3)$$

where P and P_0 are the ratios of the integrated intensities of all (00 *l*) crystal planes to those of all (*hkl*) planes for preferentially and randomly oriented samples, respectively. The calculated F value will be 1 when the grain grows exactly in the direction of the pressure. In

the present work, P and P_0 were calculated from the XRD data of a block specimen and the standard card (PDF#23–0677). The calculated result of $F_{(001)}$ is around 0.2, which reveals that the axial plane is weakly oriented.

To further confirm the phase composition of the bulk, Raman spectra have been obtained (Fig. 3). The Raman bands appear at 140.5, 205, 315 cm⁻¹, which is in agreement with the result obtained by Smith and collaborators [23]. These characteristic bands indicate that the phase composition of the bulk is 2H-SnS₂, which belongs to space group D³_{3d}-P3m1 and agrees with the standard PDF card (PDF#23–0677), see Fig. 1. Meanwhile, there is no SnS spectrum suggesting that the impure SnS phase in the precursor powder may have successfully reacted with S and was converted into SnS₂ during sintering.

Figure 4 shows an SEM image, the average elementary composition ratio and the mappings of Sn, S elements for polished surface of SnS₂ bulk, respectively. Figure 4a exhibits the morphology of the fresh fracture surface of the bulk. The bulk is seen to be almost composed of lamellar grains of diameter 10–40 μm and thickness 80–100 nm. In addition, some obvious oriented grains can be found in certain regions in the image, indicating a slight orientation in the block, which is consistent with the calculation of the orientation above. Moreover, the ratio of Sn and S elements (Fig. 4b) is nearly 1:2. The slightly higher Sn content in the composition may arise from sublimation of some S elements during sintering. During the sintering process in the present study, the vacuum is lower than 6 Pa. According to the vapor pressure calculation formula ($\log P = A - \frac{B}{t+C}$, where P stands for vapor pressure in millimeters of mercury; t is for temperature in degrees Celsius; A , B and C are constants, respectively), the temperature required for the vapor pressure of S to reach 6 Pa is 129 °C, which is much lower than the sintering temperature of 450 °C. In addition, the melting point of S element with 115.2 °C is much lower than that of Sn with 231.89 °C. Thus, these would cause the more serious deficiency of S than Sn element. Furthermore, the element mappings of Sn and S for the bulk (Fig. 4c and d) suggest that the elements are distributed homogeneously without obvious enrichment. Therefore, these results reveal that MA combining SPS is an effective and simple way to synthesize SnS₂ with a pure phase and an appropriate composition. Indeed, SnS₂ is mainly prepared by chemical vapor transport, successive ionic layer absorption and reaction, as well as other reported methods [24–26]. Compared with these methods, the two-step method used in this experiment is simpler and faster.

Figure 5 shows the TE transport properties of the SnS₂ bulk as function of temperature in the range of 300–750 K. The electrical conductivity (Fig. 5a) increases with temperature rising within the entire measured temperature range,

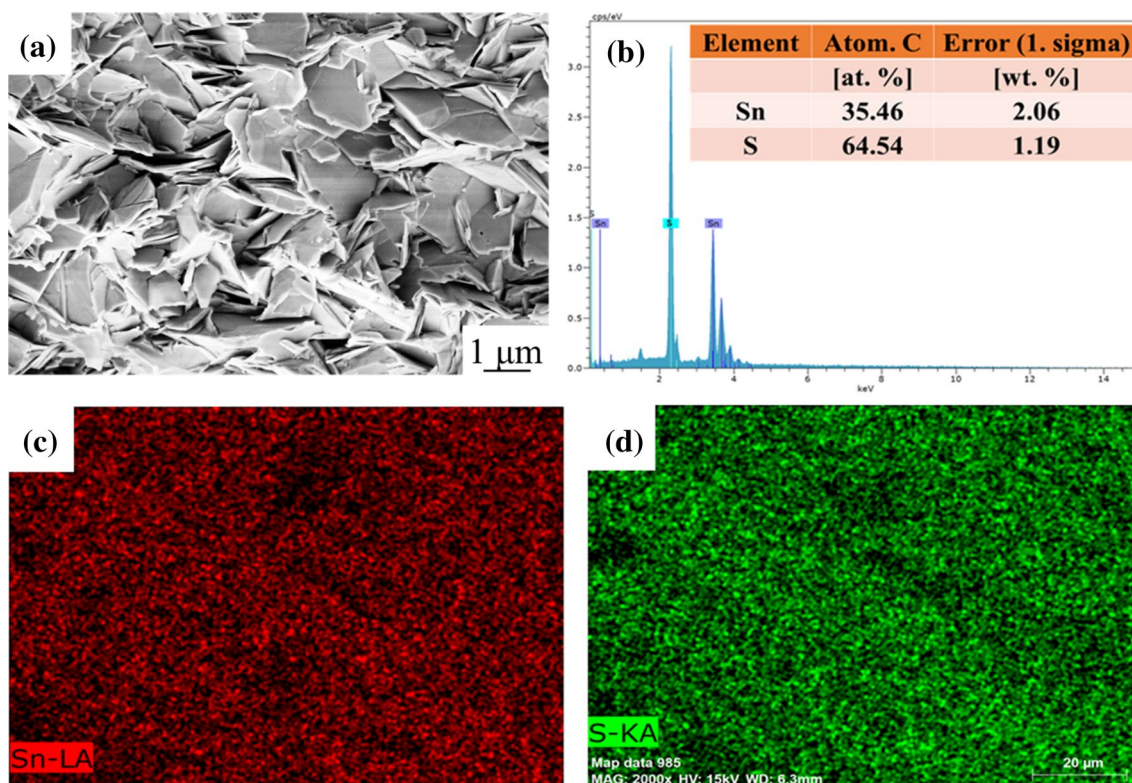


Fig. 4 **a** SEM image of SnS₂ block, **b** result of multi-point average element composition, **c** Sn element mapping of SnS₂ bulk, and **d** S element mapping of SnS₂ bulk

suggesting a typical semiconductor behavior. The value increases from 0.006 S/cm at 323 K to 0.18 S/cm at 723 K, which follows the result of Lee and collaborators that the value of electrical conductivity of SnS₂ crystals is in the range of 10⁻¹²–10⁻² S/cm [27], and is also comparable with reported values for SnSe₂ [28]. However, compared with the electrical conductivity of SnS [28] and SnSe [13], SnS₂ is a poor conductor. From the expression for electrical conductivity $\sigma = n\mu e$, where e , n , and μ are the unit charge, the carrier concentration, and the carrier mobility, the low electrical conductivity of SnS₂ stems from the low carrier concentration or carrier mobility. In addition, with increasing temperature, the carrier concentration increases because of the impact of thermal excitation, which enhances electrical conductivity with temperature rises. The Seebeck coefficient of bulk SnS₂ is negative (Fig. 5b), indicating an n-type semiconductor. The absolute value of the Seebeck coefficient also increases with temperature increases. Combined with the behavior in electrical conductivity, this anomaly may be due to the low intrinsic carrier concentration in bulk SnS₂. Numerically, the absolute value of the Seebeck coefficient rises rapidly with temperature from 75 μ V/K at 323 K to a relatively high value of 652 μ V/K at 723 K.

The calculated PF as a function of temperature (Fig. 5c) shows an increase in value with temperature. The PF

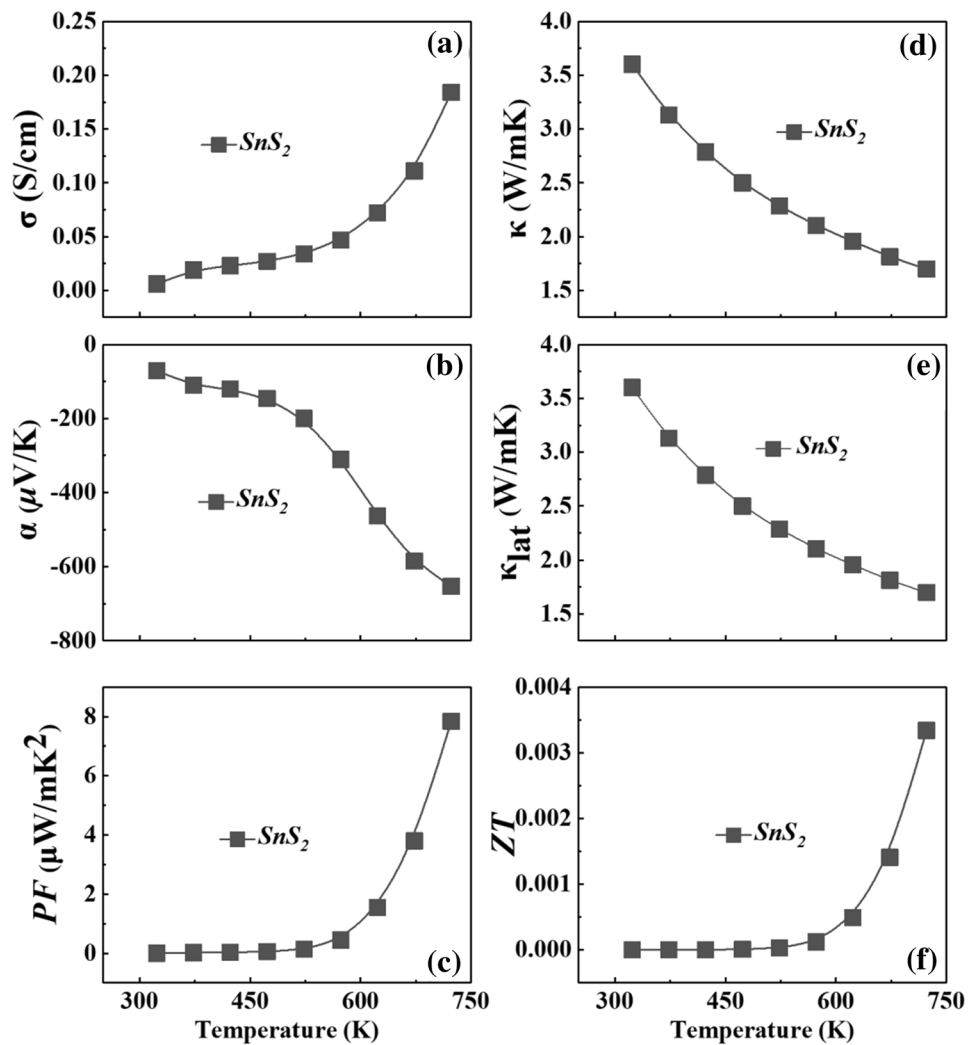
improves from 0.003 μ W/mK² at 323 K to 7.9 μ W/mK² at 723 K, benefiting from increases in both electrical conductivity and Seebeck coefficient. However, the PF of pristine SnS₂ within the entire tested temperature range is much lower compared with those for the extensively studied SnS and SnSe because of its poor electrical conductivity. Further improvements can be had by optimizing its carrier concentration.

The temperature dependence of the total thermal conductivity (κ_{total}) of SnS₂ bulk (Fig. 5d) shows that at room temperature, the κ_{total} is 3.6 W/mK which is comparable to the reported value of 3.45 W/mK of SnS₂ but slightly higher than that of SnSe₂. [27, 28] With increasing temperature, the value decreases from 3.6 W/mK at 323 K to 1.7 W/mK at 723 K. In general, κ_{total} has two contributions,

$$\kappa_{\text{total}} = \kappa_{\text{lat}} + \kappa_{\text{el}}, \quad (4)$$

in which κ_{lat} denotes the lattice thermal conductivity and κ_{el} the electronic thermal conductivity calculated using the Wiedemann–Franz–Lorenz relation $\kappa_{\text{el}} = L\sigma T$. Reduced Fermi energy was used to calculate the Lorenz number (L) (Eq. (5)) which varies as the Seebeck value changes (Eq. (5)) with temperature or composition. The

Fig. 5 Temperature dependence of thermoelectric properties of the SnS₂ block: **a** electrical conductivity, **b** Seebeck coefficient, **c** power factor, **d** thermal conductivity, **e** lattice thermal conductivity, **f** ZT values



Lorenz number L is estimated in a traditional single parabolic band model using

$$L = \left(\frac{\kappa_b}{e}\right)^2 \left\{ \frac{\left(r + \frac{7}{2}\right) F_{r+\frac{5}{2}}(\eta)}{\left(r + \frac{3}{2}\right) F_{r+\frac{1}{2}}(\eta)} - \left[\frac{\left(r + \frac{5}{2}\right) F_{r+\frac{3}{2}}(\eta)}{\left(r + \frac{3}{2}\right) F_{r+\frac{1}{2}}(\eta)} \right]^2 \right\} \quad (5)$$

$$s = \pm \frac{\kappa_B}{e} \left[\frac{\left(r + \frac{5}{2}\right) F_{r+\frac{3}{2}}(\eta)}{\left(r + \frac{3}{2}\right) F_{r+\frac{1}{2}}(\eta)} - \eta \right], \quad (6)$$

where η denotes the reduced chemical potential, r the scattering factor, and k_B the Boltzmann constant. The calculated value of L shows a deviation of less than 10% compared with those from a more rigorous single non-parabolic band and multiple band model calculations.

The contribution κ_{lat} was obtained by subtracting κ_{el} from κ_{total} . The plot κ_{lat} as a function of temperature in the

range from 300 to 723 K (Fig. 5e) shows κ_{lat} decreases with rising temperature. Moreover, κ_{lat} contributes over 90% to κ_{total} for the pristine sample, indicating heat transport in SnS₂ is dominated by phonons. However, the value of κ_{lat} is significantly higher than that of SnSe₂ [28], which has a similar-layered crystal structure and composition. Usually, thermal conductivity for different materials shows a strong dependence on the speed of sound, which is mainly associated with atomic bonding strength and scales with Young's modulus. Phonons are transported faster if the chemical bonding strength between atoms is stronger. Therefore, to verify this higher value in thermal conductivity, the speed of sound associated with longitudinal (v_l) and shear (v_s) waves in SnS₂ were measured via ultrasonic pulse echo measurements. Young's modulus was also calculated using

$$E = \frac{\rho v_s^2 (3v_l^2 - 4v_s^2)}{(v_l^2 - v_s^2)}, \quad (7)$$

where ρ denotes the density, and V_l and V_s denote the speeds associated with longitudinal and shear sound waves. The average speed (v_a) is obtained from

$$v_a = \left(\frac{1}{3} \left(\frac{1}{v_l^3} + \frac{2}{v_s^3} \right) \right)^{-1/3} \quad (8)$$

However, the calculated result shows that this average speed of sound for SnS_2 is 1869 m/s, giving Young's modulus of 32.1 Gpa, which is slightly lower than that of SnSe_2 (38.5 Gpa). Therefore, this does not seem to explain the higher thermal conductivity of SnS_2 . Generally, a layered structure subject to van der Waals interactions does support a low thermal conductivity as phonon scattering may be enhanced between weakly bonded layers. Thus, further study combined with theoretical calculations needs to be undertaken to clarify the higher thermal conductivity of SnS_2 . Combined with the electrical and thermal conductivity, the calculated ZT values of SnS_2 block was plotted (Fig. 5f). The ZT value increases with increasing temperature mainly because of the enhanced electrical transport. However, because of the low PF and high thermal conductivity, the maximum ZT only reaches 0.003 at 723 K.

It was reported that Ag is an effective dopant to improve the electrical conductivity of SnSe_2 because of significant increases in carrier concentration [28]. Meanwhile, κ_{lat} can be suppressed by the strengthened phonon scattering. Hence, to optimize the TE performance of the SnS_2 block, which shows very similar composition and crystal structure with SnSe_2 , we doped it with Ag, which is an n-type dopant in the interstitial sites in the lattice. From the XRD patterns and the magnified plots of the main peaks of the SnS_2 and $\text{SnS}_2\text{-Ag}$ blocks (Fig. 6), there are no second phase peaks in the XRD patterns for the doped sample. They all could be indexed to

the standard PDF card of SnS_2 (PDF#23–0677). Moreover, the main peak (Fig. 6b) shows that, the crystal plane peak (001) in the XRD pattern of the doped sample gradually shift toward lower 2θ angle. According to the Bragg equation ($n\lambda = 2d\sin\theta$), the shift of the X-ray diffraction peak to a small angle indicates that the distance of crystal face increases. Thus, the shift of the XRD pattern in the present study suggests the lattice parameter increases after Ag doping. The lattice parameter values were estimated from step-scan XRD measurements with step width of 0.02° using the least-squares method. A smooth surface of the bulk was polished well before taking XRD measurements of doped samples to obtain much more accurate X-ray peaks. The calculated lattice spacings along the a-axis for pure and doped sample are, respectively, 3.6521 and 3.6543 Å, whereas for the c-axis are 5.9136 and 5.9253 Å, which indicates the lattice parameters increased after Ag doping. However, the atomic radius of Ag with 1.44 Å is smaller than that of Sn with 1.58 Å. These results prove that the increase of the lattice parameter of the Ag-doped sample is probably caused by the entry of Ag element into the SnS_2 lattice gap. Furthermore, the composition and distribution of Ag were obtained by EDS on the polished surfaces of the Ag-doped sample showing Ag was distributed inhomogeneous. A slight Ag enrichment was observed in some areas. No peaks of the secondary phase appeared in the XRD patterns probably because its content was low.

Furthermore, we have also characterized the TE properties of doped sample (Fig. 7). The conductivities of doped and pristine samples both show trends of increasing with temperature (Fig. 7a). The conductivity of $\text{SnS}_2\text{-Ag}$ is lower than pure phase before 573 K. With the increase of temperature, it crosses with SnS_2 at 573 K and increased significantly after that. The maximum conductivity reached 0.49 S/m at 723 K which is about three times that of pure sample. On the other hand, different from SnS_2 , the absolute value of Seebeck coefficient of $\text{SnS}_2\text{-Ag}$ shows a decreasing trend with temperature rise. The value drops to 664 $\mu\text{V/K}$ at 723 K, which is closed to the SnS_2 (Fig. 7b). According to the results of phase characterization, the reason may be that, the lattice distortion caused by Ag interstitial doping increases the scattering of carriers and reduces the conductivity at low temperature. However, Ag doping also increased carrier mobility, making the absolute Seebeck coefficient significantly increased. With the increase of temperature, more activation energy can increase carrier concentration and reduce the influence of scattering on them. At the same time, the defects brought by Ag doping also introduced more carriers at high temperature so that the conductivity of doped samples gradually increased, while the Seebeck coefficient dropped. Further, mainly affected by the change of electrical conductivity, the PF shows a trend of positive correlation with temperature. The optimal value of 22 $\mu\text{W/}$

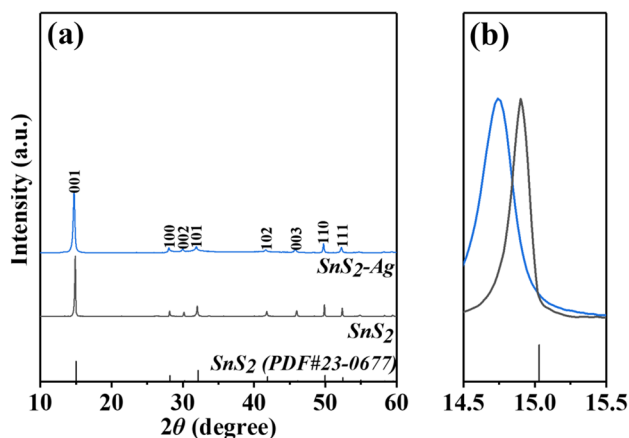
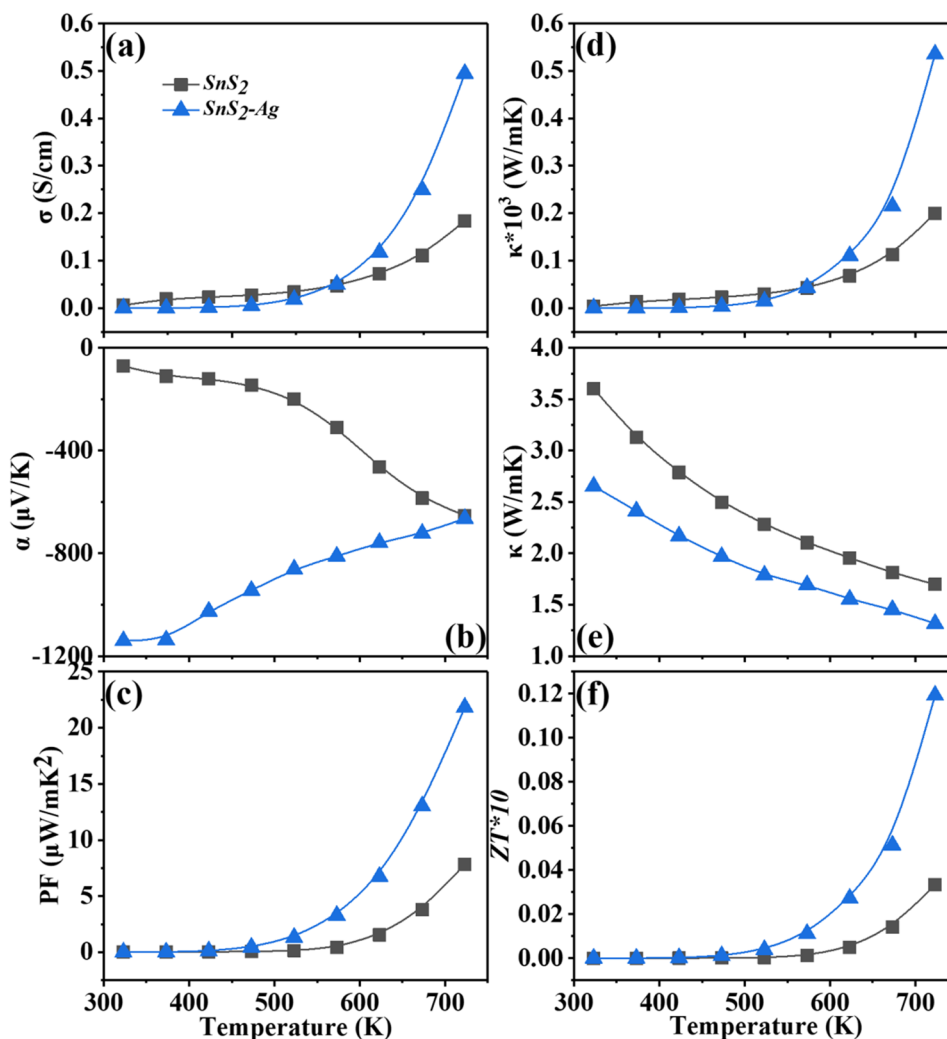


Fig. 6 XRD patterns and main peak magnifications of SnS_2 and $\text{SnS}_2\text{-Ag}$ block

Fig. 7 Thermoelectric properties of SnS₂ and SnS₂-Ag sample: **a** electrical conductivity, **b** Seebeck coefficient, **c** power factor, **d** thermal conductivity, **e** lattice thermal conductivity, **f** ZT



mK^2 was obtained at 723 K, which was about three times of the pure phase (Fig. 7c). The dependence of κ_e on temperature (Fig. 7d) displays an obviously increase and, after Ag doping, κ_e shows the same trend as electrical conductivity, which may also affect by carrier concentration. Numerically, κ_e is far less than κ_{total} , indicating that the κ_{total} of samples are mainly composed of κ_{lat} . The κ_{total} of the samples shows a significant trend of decrease with temperature (Fig. 7e). However, influenced by the rise of κ_e , the decline trend of SnS₂-Ag's κ_{total} slowed a little after 573 K. After doping, the value at room temperature is reduced from 3.6 W/mK for the SnS₂ to 2.7 W/mK for the SnS₂-Ag sample. When the temperature rises to 723 K, κ_{total} has the lowest value of 1.3 W/mK for the SnS₂-Ag sample. The calculated κ_e suggests that the reduced κ_{total} is mainly caused by the decrease in κ_{lat} . Lattice distortions caused by substitutive and interstitial Ag atoms together enhance short-wave phonon scattering, which may be the main reason for the reduced κ_{lat} . This indicates that Ag doping can increase phonon scattering effectively and reduce the thermal conductivity of the

samples. With the benefit of an enhanced PF and reduced κ_{lat} , an improved ZT value was obtained (Fig. 7f). A maximum value of 0.01 at 723 K was achieved for the SnS₂-Ag sample and was two times higher than the value for SnS₂ at the same temperature. These results indicate that Ag is an effective dopant to enhance the TE property of SnS₂. Higher ZT values are expected by further doping experiments.

3 Conclusion

SnS₂ was synthesized by combining MA with SPS. The synthesis process and the TE properties over the temperature range 300–723 K were investigated. The results indicate that SnS₂ bulk with pure phase is obtained after sintering the precursor powder, although single-phase SnS₂ powder seems difficult to obtain by MA because Sn₂S₃ is produced with prolonged milling times. Pristine SnS₂ bulk shows an n-type conductive characteristic and a moderate absolute Seebeck coefficient in the range 100–700 $\mu\text{V/K}$. However,

the electrical conductivity below 0.2 S/cm is poor and the thermal conductivity above 1.5 W/mK is relatively high, resulting in a low ZT value. Nevertheless, after Ag doping, both the electrical resistivity and thermal conductivity have been reduced within the entire measured temperature range. Therefore, an enhanced ZT compared with the pristine sample was obtained.

Acknowledgements This work was supported by the Fund of Natural Science Foundation of Guangdong Province (No. 2018A030313574) and Shenzhen Science and Technology Plan Project (No. JCYJ20170818142740568), as well as Shenzhen Key Lab Fund (No. ZDSYS20170228105421966). We thank Richard Haase, Ph.D, from Liwen Bianji, Edanz Group China (www.liwenbianji.cn/ac), for editing the English text of a draft of this manuscript.

References

- P. Zong, R. Hanus, M. Dylla, *Energ. Environ. Sci.* **10**, 1 (2017)
- M. Ziabari, D. Zebajadi, Vashae. *Rep. Prog. Phys.* **79**, 9 (2016)
- X. Zhang, L.D. Zhao, *J. Materiomics* **1**(2), 92–105 (2015)
- G. Tan, L.D. Zhao, M.G. Kanatzidis, *Chem. Rev.* **116**, 19 (2016)
- B. Russ, A. Glauddell, J.J. Urban et al., *Nat. Rev. Mater.* **1**, 10 (2016)
- J.R. Sootsman, D.Y. Chung, M.G. Kanatzidis, *Angew. Chem. Int. Edit.* **48**, 46 (2009)
- C. Chang, Wu, M. Wu, He, D. He, et al., *Science*, 360(6390), 778–783 (2018).
- J. Zhang, L. Song, G.K.H. Madsen et al., *Nat. Commun.* **7**, 10892 (2016)
- B. Asfandiyar, L.-D. Cai, J.-F. Zhao, J. Li, *Materiomics* **6**(1), 77–85 (2020)
- J.N. Coleman, M. Lotya, A. O'Neill, *Science* **331**, 6017 (2011)
- M. Lee, L. Viciu, L. Li, *Nat. Mater.* **5**, 7 (2006)
- Y. Terasaki, K. Sasago, Uchinokura. *Phys. Rev. B* **56**, 20 (1997)
- S. Bresch, B. Mieller, C. Selleng, *J. Electroceram.* **40**, 3 (2018)
- L.-D. Zhao, S.-H. Lo, Y. Zhang, H. Tan et al., *Nature* **508**, 7496 (2014)
- B. Ouyang, S. Chen, Y. Jing, T. Wei, S. Xiong, D. Donadio, *J. Materiomics* **4**(4), 329–337 (2018)
- W. Xie, J. He, H.J. Kang, X. Tang, S. Zhu, M. Laver et al., *Nano Lett.* **10**(9), 3283–3289 (2010)
- G. Guélou, P. Vaqueiro, J. Prado-Gonjal, *J. Mater. Chem. C.* **4**, 9 (2016)
- E. Guilmeau, Y. Bréard, A. Maignan, *Appl. Phys. Lett.* **99**, 5 (2011)
- T.M. Tritt, M.A. Subramanian, *MRS Bull.* **31**, 3 (2006)
- R. Nunna, F. Gascoin, E. Guilmeau, *J. Alloys Compd.* **634**, 32–36 (2015)
- D. L. Ye, J. H. Hu, *Handbook of Practicality Inorganic Thermodynamics.* (2002).
- Z. Shen, M. Johnsson, Z. Zhao, M. Nygren, *J. Am. Ceram. Soc.* **85**(8), 1921–1927 (2002)
- J. Smith, P. E. Meek, W. Y. Liang, *J. Phys. C: Solid State Phys.* **10**, 8:1321 (1977).
- B.R. Sankapal, R.S. Mane, C.D. Lokhande, *Mater. Res. Bull.* **35**(12), 2027–2035 (2000)
- N.G. Deshpande, A.A. Sagade, Y.G. Gudage, *J. Alloy. Compd.* **469**, 1–2 (2009)
- M.-J. Lee, J.-H. Ahn, J.H. Sung et al., *Nat. Commun.* **7**, 12011 (2016)
- L.E.I.F. Brattas, & A. KJEKSHUS, *Acta Cehmica Scandinavica* **27**, 1290–1298 (1973)
- X. He, H. Shen, *Phys. B: Condens. Matter* **407**(7), 1146–1152 (2012)

Publisher's Note Springer Nature remains neutral with regard to jurisdictional claims in published maps and institutional affiliations.